RESEARCH ARTICLE

High-resolution PIV measurement over wind-generated waves

Wagih Abu Rowin[1] · Kevin[1] · Tunggul Bhirawa[2] · Will Junghoon Lee[3] · Jimmy Philip[1] · Ivan Marusic[1] · Jason Monty[1]

Abstract

The interaction between wind and waves plays a significant role in the exchange of heat, aerosols and gases, thereby influencing our understanding of climate dynamics and air–sea interaction. Particle image velocimetry (PIV) has emerged as a valuable tool for investigating the intricate effects of small-scale waves on airflow characteristics in laboratory settings. However, previous PIV experiments have exhibited notable variability in spatial resolution, potentially affecting the accuracy of turbulence statistics, particularly in relation to small-scale waves such as capillary ripples. To systematically explore the impact of PIV spatial resolution on airflow characteristics over multi-scale wind-generated waves, we conducted high-resolution planar PIV experiments near the wave surface. We adjusted the spatial resolution of the results by modifying the spatial filter. Additionally, recognising the limitations of the high-resolution PIV system in terms of wall-normal and streamwise extent, we conducted larger field-of-view experiments to capture consecutive waveforms and achieve spatial averaging across the boundary layer. Consistent with existing literature, our findings illustrate the formation of a horizontal shear layer leading to airflow separation on the lee side of the wave, accompanied by a pronounced vorticity field and circulation region. Notably, analysis of the high-magnification dataset reveals localised airflow separation caused by small-scale capillary waves, phenomena not resolved by the large field-of-view set-up, underscoring the importance of adequate spatial resolution. Further analysis indicates that a spatial resolution larger than the size of the capillary waves leads to significant attenuation of the spanwise vorticity imposed by the small-scale waves. In this study, we also introduce a novel method relying to identify wave surfaces solely on PIV images, demonstrating its effectiveness in detecting capillary-scale waves.

1 Introduction

The interaction between wind and waves at the ocean–atmosphere interface is pivotal in transferring heat, aerosols and gases such as CO_2. As a result, comprehending the intricate mechanisms that govern momentum exchanges across this interface is an area of active scientific research. To date, a wide range of field and laboratory observations have been documented, dating back to the era of Aristotle (384–322 BC) (Sullivan and McWilliams 2010; Stanislaw 2012).

Oceanic wind generates a wide range of wavelengths and frequencies, and meteorological events such as earthquakes and storms only broaden that range. These forces create a multi-scale wave surface that spans four orders of magnitude, from the capillary-gravity waves with $f \gtrsim 10$ Hz to sea swells with $f \lesssim 10^{-2}$ Hz (Stanislaw 2012; Laxague et al. 2015). In terms of energy content, wind waves of order $f \gtrsim 10^{-1}$ Hz are the most energetic, and they are often accompanied by capillary ripples atop them (Okuda 1982). It is the asymmetric surface pressure distribution in the carrier waves that continually generates these riding capillaries. Capillary ripples can vary in size from millimetres to centimetres (Zhang 1995), and they can either occur along the entire wave surface or confined to the leeward slope (Hung and Tsai 2009) as depicted in Fig. 1.

The importance of the smaller capillary waves was illustrated by Barger et al. (1970) who suppressed them using an oil layer (slick). The layer increases water surface tension and dampens the capillary formation. The findings showed increased airflow speed near the wave surface in the absence of the capillary waves. Since then, there has been increasing interest in elucidating the importance of small waves to sea drag and their impact on the turbulent wind (e.g.

✉ Wagih Abu Rowin
aburowin@ualberta.ca

1 Department of Mechanical Engineering, University of Melbourne, Parkville, VIC 3010, Australia

2 Marine Biophysics Unit, Okinawa Institute of Science and Technology, Onna-son, Okinawa 904-0495, Japan

3 Platforms Division, Defence Science and Technology Group, Canberra, VIC 3207, Australia

Okuda 1982; Longuet-Higgins 1987, 1992; Mui and Dommermuth 1995; Donelan et al. 2004; Lin and Perlin 2001; Mueller and Veron 2009,). However, field observations of small waves are challenging due to the large range of wave scales at sea, compounding the practical difficulties such as instrument access and the harsh and corrosive marine environment. Almost all field observations of turbulent wind are collected with sensors located at fixed heights, limiting the ability to capture detailed flow information close to the surface (Pizzo et al. 2021). Therefore, controlled laboratory experiments are key to investigating the small-scale waves and their influence on the wave characteristics (Banner and Melville 1976; Reul et al. 1999; Liu et al. 2004; Grare et al. 2013; Buckley and Veron 2017; Geva and Shemer 2022; Porchetta et al. 2022).

Even in the laboratory, obtaining simultaneous airflow and wave height measurements over the full range of wavelengths is non-trivial. More recently, researchers have employed particle image velocimetry (PIV) as a non-intrusive flow measurement technique, where aerosols are introduced to the airflow as tracers. In a typical set-up, a laser light sheet will illuminate the particles where they are imaged by a camera (Banner and Peirson 1998; Lin and Perlin 2001; Liu et al. 2004; Sveen and Jensen 2004; Reul et al. 2008; Buckley and Veron 2016, 2017; Porchetta et al. 2022). The velocity information is then obtained by comparing two consecutive particle images via cross-correlation. The main advantage of PIV technique is that it provides maps of instantaneous velocities in 2D (or sometimes 3D). One aspect to consider in a PIV configuration is the trade-off between the size of the field-of-view (FOV) and the resulting image resolution. In a typical PIV set-up with a single camera, it is not possible to obtain a large FOV (across multiple carrier waves) while simultaneously resolving fine-scale eddies shed by the capillary ripples. Poor image resolution typically affects PIV measurement in two ways. The first is the inability to capture small-scale turbulent motions, resulting in an underestimation of turbulence statistics such as Reynolds shear stress. The second is the inability to resolve information close to a surface, due to the light reflection from the surface.

In wind-wave analysis, the need for adequate spatial resolution is critical. This significance was demonstrated by the numerical simulations of Hung and Tsai (2009), where they systematically varied the computational grid resolution. Notably, larger grid sizes resulted in the unresolved representation of capillary waves, accompanied by an attenuation of their influence, particularly in the vorticity field. Nonetheless, past PIV experiments on wind waves had been performed with a variety of spatial resolutions, spanning from ~10 viscous units (Buckley and Veron 2016; Porchetta et al. 2022) to ~200 viscous units in works like in Reul et al.

(2008) and Buckley and Veron (2017). The effect of spatial resolution is yet to be properly addressed.

Conducting PIV measurements over wind waves presents a significant challenge compared to PIV measurements over a solid stationary body, primarily due to the dynamic nature of the water surface. Images obtained from PIV measurements conducted on the water side of the waves often exhibit multiple bright regions near the wave surface, stemming from light reflecting off seeding particles floating at the surface, ghost particles caused by the combination of camera angle and the angle of the water-to-air interface, and/or strong reflections from the free surface location (Zarruk 2005; Sanchis and Jensen 2011; Dussol et al. 2016). These challenges complicate the detection of the water surface and consequently hinder velocity measurements in the vicinity of the wave surface. To address these challenges, several methods have been developed in the literature to estimate the wave surface solely from PIV images obtained on the water side (Zarruk 2005; Lin and Perlin 1998; Jeon and Sung 2011). However, detecting the wave surface for PIV measurements conducted on the air side over waves presents additional challenges (Buckley and Veron 2017). Unlike PIV measurements on the water side of the waves, where the wind field above the waves leads to minimal reflections, air side PIV measurements over waves encounter unsteady reflections of the laser sheet due to the water surface and its small variations, as depicted in the sample image in Fig. 1. Factors such as spray bubbles in high winds and meniscus effects (where the three-dimensionality of the waves causes visual blockage) can further complicate the detection of the wave surface. To overcome these challenges and detect the air–water interface for PIV measurements on the air side over waves, some studies have incorporated an additional imaging system alongside their PIV set-up. For instance, Buckley and Veron (2017) utilised a laser-induced fluorescence system, while Porchetta et al. (2022) released dye
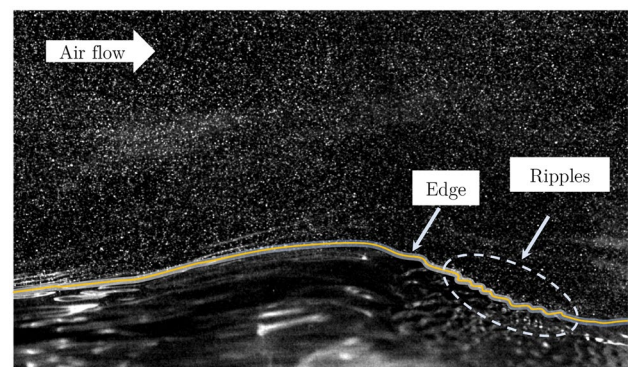
Fig. 1 A close-up photograph of the wind-wave structures. The air side is seeded with particles for PIV measurement, and the flow direction is from left to right as indicated by the arrow. The solid line is outlying the wave and showing the wave edge and the ripples

on the water surface and captured images using a separate camera.

In this study, our objective is to introduce a method for identifying wave surfaces from the PIV (particle) images. This method can detect wave surfaces down to the capillary scale, provided high-resolution images are available. We will provide comprehensive details on the procedures involved, and the codes will be made publicly accessible. To investigate the influence of small waves on the flow, we conducted high-magnification PIV measurements to capture turbulent motions and separation phenomena close to the wave surface, albeit within a confined streamwise–wall-normal plane. Additionally, a large FOV is acquired to understand the larger-scale flow patterns, including flow over consecutive waveforms, and to obtain resolved spatial averages. The resulting data sets acquired are used to analyse turbulent flow characteristics, comment on velocity scaling and provide some insight into small-scale flow kinematics crucial to the interaction between wind and waves.

2 Measurement facility and wind-wave parameters

2.1 Wind-wave facility

The experiments are conducted at the sea ice–wind-wave interaction facility located in the Michell Hydrodynamics Laboratory at the University of Melbourne. The facility consists of a wave flume housed within an insulated room where temperature can be controlled down to -18 °C, although this particular study is conducted under ambient conditions (approximately 25 °C). The dimensions of the wave flume are 14 m in length, 0.75 m in width and 0.7 m in height, in the streamwise (x-), spanwise (y-) and wall-normal (z-) directions, respectively, see Fig. 2. At the downstream end of the flume, a permeable sloped beach is installed (see Fig. 2a) to dissipate the incoming waves. Glass walls, floor and perspex ceiling in the flume allow for complete optical access to the test section.

The upper portion of the wave flume is formed by a suction-type wind tunnel. The wind is generated by a mixed-flow duct fan capable of delivering airflow up to 4.5 m^3 s^{-1}. The wind-tunnel entrance is equipped with a bell mouth to smoothen the air intake, reducing acoustic noise and pressure losses. The airflow then passes through a honeycomb flow straightener and perforated screens, which further remove larger-scale turbulence. A contraction with an area ratio of 3:1 leads to the test section. The freestream turbulence intensity, recorded using hot-wire anemometry, at the PIV location (at 3.5 m fetch), is nominally 0.5%. The flume is filled with water to a depth of 0.3 m, leaving a wind-tunnel test section (referred to as the air side) of 0.4 m in height

extending up to the ceiling. It is ensured that the boundary layer thickness (δ) remains less than 30% of the air side column to prevent flow interaction from the roof (becoming a channel/duct flow) and minimise pressure gradient in the streamwise direction. The boundary layer thickness δ over the waves is defined as the height where the mean streamwise velocity $\langle U \rangle$ recovers to 99% of the freestream velocity ($\langle U \rangle = 0.99 U_{\infty}$). Here, the subscript '$\infty$' refers to freestream quantities and the angle brackets '$\langle . \rangle$' denotes quantities averaged in x-directions and time t. The freestream velocity is determined using a Pitot tube installed from the tunnel ceiling. The measurement uncertainty of U_{∞} ($\epsilon(U_{\infty})$), computed via propagation of error as detailed in Appendix A, is $\epsilon(U_{\infty}) = \pm 125$ mm^{-1}.

2.2 Pressure gradient in the wind tunnel

The wind-wave development process entails the growth of boundary layers, resulting in a reduction of the effective height and the cross-section of the wind tunnel. Consequently, the airflow within the tunnel experiences acceleration (favourable pressure gradient), which will affect both the mean velocity and the Reynolds stress values (see, for example, Harun et al. 2013). To reduce this effect, the roof panels of the wind tunnel are positively inclined. Even still, a series of static pressure taps installed in the streamwise direction on the tunnel roof measured a slight decrease in static pressure, characterised by a gradient of $dC_P/dx = -0.028$, here $C_P = (p_{\text{ref}} - p)/(0.5\rho U_{\infty}^2)$ represents the static pressure coefficient (Fig. 2b). Here, p denotes the static pressure at each streamwise location, while p_{ref} is the reference pressure signal recorded at $x = 3.5$, where the measurements are conducted and ρ is the air density. The error bars in Fig. 2b are computed from the propagation or error as discussed in Appendix A. The pressure gradient in this study can be categorised as "mild", and its impact on the large-scale structures is expected to be insignificant (Harun et al. 2013).

2.3 Wind-wave parameters

The wind waves are generated over a fetch of 3.5 m with freestream velocity of $U_{\infty} = 5.6$ m s^{-1}. Visual observations reveal a range of wave types, starting from small capillaries to gravity waves characterised by gentle spilling breakers. To capture the temporal fluctuations of waves, General Acoustics ULTRALAB ULS HF58 ultrasonic sensors are employed with a resolution of 180 μm, sampling at a frequency of 100 Hz. Examples of surface fluctuations are presented in Fig. 3a. The root mean square of the wave height is $k_{\text{rms}} \approx 2.1$ mm, whereas the dominant wave height is $k_0 \approx 8.8$ mm. The subscript '0' refers to the properties of the dominant wave. The frequency of the dominant waves is

(a) bellmouth

(b)
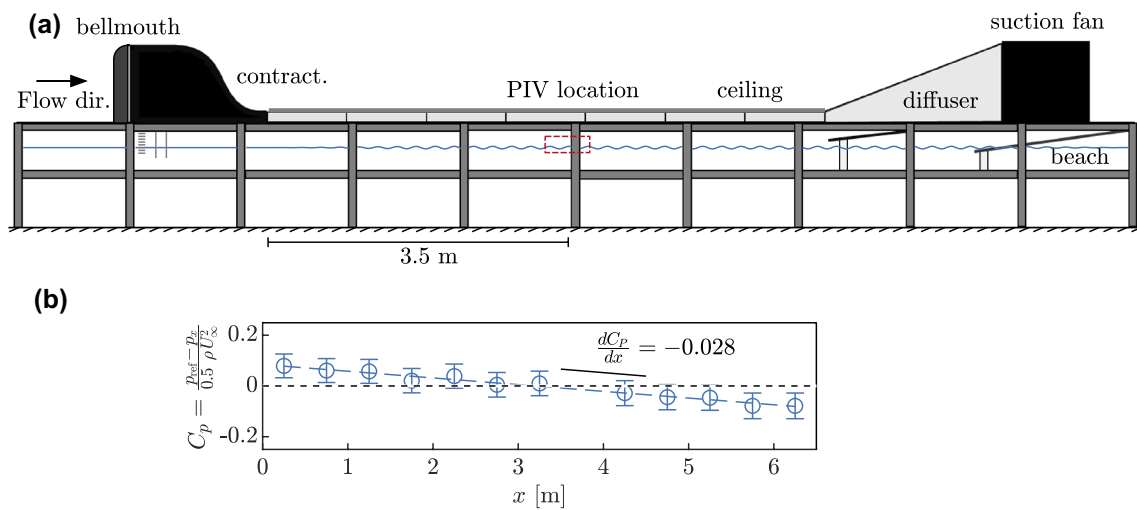
Fig. 2 **a** Schematic showing the sea ice–wind-wave interaction facility, including the wave flume, suction-type wind tunnel and the measurement location at 3.5 m fetch. **b** The distribution of static pressure coefficient C_p along the wind tunnel at wind speed $U_\infty = 5.6$ m s^{-1}. The subscript 'ref' in C_p definition denotes parameters evaluated at the PIV station location. Error bars in **b** illustrate the measurement uncertainty

clearly visible through the spectral peaks S_{kk} depicted by a '+' mark in Fig. 3b. The broad spectral distribution signifies the irregular nature of the wind waves. The wave parameters are summarised in Table 1, with the phase velocity of the dominant waveform C_0 extracted from the spatiotemporal data obtained by Bhirawa et al. (2018) for the same flow case. Physically, the dominant waves travel at approximately 8% of U_∞.

3 PIV experiments

Two separate planar PIV experiments in a streamwise/vertical configuration are conducted. The first is a high-magnification PIV (HM-PIV) configuration, designed to accurately resolve turbulent motions and separation events but in a limited streamwise extent. Importantly, better spatial resolution minimises the underestimation of turbulence statistics and, hence, the sea drag value. The second set-up is a large field-of-view (LF-PIV) configuration, aimed to capture a larger domain encompassing multiple waveforms, albeit at a lower resolution. Both PIV set-ups utilised two PCO4000 cameras with 14-bit depth and 11-megapixel resolution. These camera systems are depicted in Fig. 4a, b. It is important to acknowledge that while these PIV systems were not performed simultaneously, their outcomes work together to offer a comprehensive understanding of airflow characteristics both in close proximity to and further away from the wave surface.
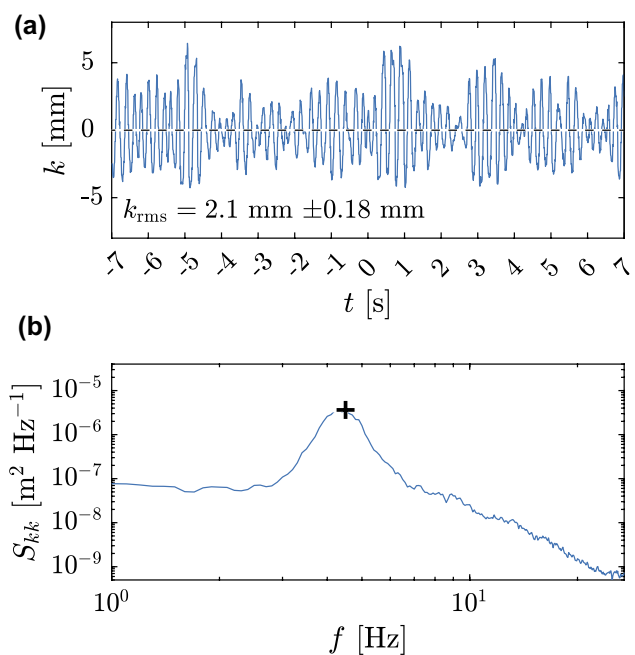
Fig. 3 **a** Examples of wave-height fluctuation signal $k(t)$ at $x \approx 3.5$ m fetch. The root mean square (rms) is indicated by k_{rms}. **b** Power spectral densities of the wave height S_{kk} using the ultrasonic sensor. The '+' mark in **b** is at the spectra peak

In order to visualise the airflow, we introduced 1–4μm diameter fog tracers into the air stream, illuminated by a 0.5-mm-thick laser sheet generated by a Quantel EverGreen Nd:YAG laser. The cameras in Fig. 4a, b are positioned at a 5° downward angle. This arrangement was chosen to

mitigate potential obstructions caused by wave crests that may block part of the measurement plane from the camera (Lin and Perlin 1998), as will be discussed in Sect. 3.3. Such challenges are inherent in image-based measurements, particularly when dealing with three-dimensional surface topography.

To compensate for lens and viewing-angle distortions, the acquired images from the cameras undergo a calibration process using precisely located dots. The dots are uniformly spaced at 5-mm intervals in both the streamwise and wall-normal directions. It is essential to capture the calibration image when the water level is substantially lower than the still water level, to ensure adequate coverage in the deepest troughs of the waves. The evaluation and reconstruction of displacements in the PIV measurements are conducted using an in-house PIV package previously employed by Kevin et al. (2019) and others.

The uncertainty inherent in PIV measurements may result from various sources, including the displacement of interrogation windows due to 'sub-pixel' offset, spatial resolution and detection of wall location, relevant for wave surface detection in this study, (Lecordier et al. 2001; Astarita and Cardone 2005; Kähler et al. 2012). These distinct sources of error can impact the time-averaged statistical parameters, such as mean, standard deviation and variance, as demonstrated by Sciacchitano and Wieneke (2016). Given the complexity of the processing steps involved in deriving statistical quantities from PIV images, we adopted a generalised uncertainty estimation method proposed by Moffat (1988). The details of this method and the resulting uncertainties are provided in Appendix A.

3.1 High-resolution measurements (HM-PIV)

To resolve the turbulent motions across the boundary layer above waves, two cameras (C_1 and C_2) are arranged to create a vertical FOV spanning 50×150 mm in the $x \times z$ directions, as depicted in Fig. 4a, c. The top camera, C_1, is equipped with a Sigma 105 mm macro-lens, providing a resolution of ~ 40 μm pix^{-1}. The lower camera, C2, employs a Tamron 180-mm macro-lens and extension rings to capture a higher resolution of ~ 17.8 μm pix^{-1}. A total of 1500 independent velocity realisations are recorded for each experiment.

Given that C_1 and C_2 cameras have different resolutions, we adjusted the interrogation window size to achieve a comparable resolution in real space. C_1 is analysed with an interrogation window of 24×24 pixels^2 while C_2 with 56×56 pixels^2, both with 50% overlap. This adjustment, when considering the thickness of the laser sheet (0.5 mm), yielded a viscous-normalised (e.g. $z^+ = zU_\tau/\nu$) spatial resolution of $18 \times 10 \times 18$ in the streamwise, spanwise and wall-normal directions.

Additionally, we performed specific processing of the images acquired by the C_2 camera to enhance resolution in the proximity of the waves. In this scenario, the C_2 images are assessed using an interrogation window of 16×16 pixels^2, with 50% overlap, resulting in normalised spatial resolutions of $10 \times 10 \times 10$. It is important to avoid noisy velocity fields caused by low vector correlations, as they can artificially inflate turbulence intensity and Reynolds shear stress values (Atkinson et al. 2014).

3.2 Large field-of-view measurements, LF-PIV

The primary aim of this configuration is to capture the larger turbulent motions occurring in the outer layer, which can extend across multiple dominant wavelengths. The results derived from this set-up also serve as a foundation for conditional averaging over specific wave sizes, allowing for an investigation into the dispersive stresses and wave boundary layer associated with the dominant waves. To realise this objective, we employ two cameras positioned side-by-side, as shown in Fig. 4b, which provides a wide FOV. Both cameras, C_1 and C_2, are equipped with Sigma 105-mm macro-lenses, resulting in a digital resolution of 54 μm pix^{-1}. The reconstructed view of the measurement domain is depicted in Fig. 4d, highlighting a streamwise extent of ≈ 400 mm, approximately equivalent to 4.8δ. In this configuration, we utilise a final interrogation window of 24×24 pixels^2, thereby achieving a viscous-scaled spatial resolution of $25 \times 10 \times 25$. The data collection from this PIV experiment yields a total of 1200 reconstructed velocity realisations.

3.3 Determining air–water interface

Performing PIV measurements near a surface or boundary is inherently challenging, due to light reflection. However, in the current scenario, these challenges are further compounded by the presence of three-dimensional waves, which introduces the potential for view obstructions at the measurement location, and the dynamic nature of the waves. Consequently, it becomes imperative to accurately identify the air–water interface before conducting PIV vector processing. This interface detection serves the purpose of delineating and masking the "invalid" regions during PIV processing and subsequent data analysis. While simultaneous laser-induced fluorescence techniques, as demonstrated by Buckley and Veron (2016), can provide valuable assistance in interface detection, the detection process is performed with PIV images only. The procedure for interface detection is depicted for an example particle image in Fig. 5a, and described below. The developed Mathworks MATLAB code, employed for executing the steps to identify the air–water

interface, has been made accessible on our GitHub repository (Abu Rowin and Kevin 2023).

1. The dual-frame PIV pairs are combined to double the intensity at the air–water interface. This is justified by the negligible wave movements relative to the time difference of approximately 50 µs between the frames.
2. The combined image is subjected to a high-pass filter to eliminate large features such as bubbles and droplets, yielding the result shown in Fig. 5b.
3. The intensity values are squared to enhance the contrast between the particles and background, resulting in Fig. 5c.
4. A low-pass filter is applied to the image using a small rectangular kernel, as shown in Fig. 5d. This process further enhances the contrast and horizontally fills the air–water interface.
5. The intensity jump is detected by identifying the maximum change of the root mean square of the intensity for each column of pixels, as indicated by the red dots in Fig. 5e.

Table 1 Surface waves parameters performed at fetch of $x = 3.5$ m

U_∞ [m s^{-1}]	k_0 [mm]	k_{rms} [mm]	C_0 [m s^{-1}]	λ_0 [mm]	C_0/U_τ –
5.6	8.8	2.1	0.47	108	1.69

The waves parameters include: the dominant wave height (k_0), root mean square of the wave height (k_{rms}), the phase velocity of peak wave frequency (C_0) and the wave age (C_0/U_τ)

6. Piecewise polynomials are then fitted through the detected points on the surface, yielding a continuous representation of the interface. An example of the detected surface is depicted by the solid line in Fig. 5f, with the dashed lines indicating a region of ± 0.5 mm. This region is considered as a source of uncertainty from the current surface detection method and utilised in the uncertainty analysis in Appendix A. In order to identify outliers and retain data points to be used for the final wave surface fit (shown as green points in the left inset of Fig. 5f), we applied the Hampel identifier method with limits set at 1.5 standard deviations, a choice informed by initial analysis. We then retained data points whose local median fell within these specified limits.

The last step involves removing any instances of wave-blocking effects, specifically the visual obstruction of 3D wave. This is accomplished by evaluating the displacement of particles directly above the water surface. The occurrence of this issue is exemplified in Fig. 6a, which illustrates how wave crests intermittently manifest between the camera sensor and the object plane, obstructing the true water surface and obscuring the airflow information. Figure 6b depicts a frame in which the left side exhibits a valid and well-defined interface, while the right side is affected by a blurring problem. Consequently, the particle displacements immediately above the valid surface (left side), as shown in Fig. 6c, are minimal, whereas those above the erroneous region (right side) exceed the predetermined threshold of ~ 3 pixels. To effectively identify and flag invalid regions, we establish a criterion based on the width of the detected region. Specifically, when the width exceeds 8 mm, we deem the region to be invalid. Employing this criterion results in approximately 18% of images are discarded. Changing the threshold values ranging from 2 to 5 pixels or ± 2 mm from the initial ~ 3 pixels or ~ 8 mm did not significantly affect the obtained results.

3.4 The spatial properties of the wind waves

An example of a wave surface extracted from a high-resolution PIV (HM-PIV) experiment is shown in Fig. 7a. The symmetry of the waveforms (θ), depicted in the figure, is computed as the angle formed between a horizontal line and a tangent drawn along the wave surface. The probability density function (*pdf*) of θ is shown in Fig. 7b. The error bars in this figure are obtained for the uncertainty in the wave surface detection, as discussed in Sect. 3.3. Figure 7b reveals a longer negative tail in the *pdf*, describing the asymmetry of wind wave, which has a steeper slope on the leeward face of the wave crest, or in other words, the waveform tends to lean towards the direction of its propagation. Such a wave steepness directly influences the intensity of the local adverse pressure gradient, which in turn affects the likelihood of separation events (Reul et al. 2008).

To obtain the spatial properties of wind waves, such as wave height and skewness (*SK*), we plot the *pdf* of the wave-height (k) fluctuation obtained from the high-resolution PIV (HM-PIV) and the reference ultrasonic sensor. In Fig. 8a, the standard deviation $k_{rms} = 9.8$ cm and the positive skewness of the waves (*SK* = 0.52) illustrate the common attributes of deep water waves, namely that the crests are high and sharp while the troughs are shallow and flat (Holthuijsen 2010). The good agreement between the PIV results (solid line) and the reference ultrasonic sensor (dashed line) affirms the reliability of the PIV measurements in capturing significant wave properties.

To understand the wave patterns, Fig. 8b shows the spatial spectra of wave energy S_{kk} from HM-PIV and LF-PIV obtained from the detected waves in each realisation. The results indicate that HM-PIV, represented by the thick lines, has more wave energy compared to LF-PIV. This is because HM-PIV can capture surface fluctuations better,

(a)

(b)

(c)

(d)
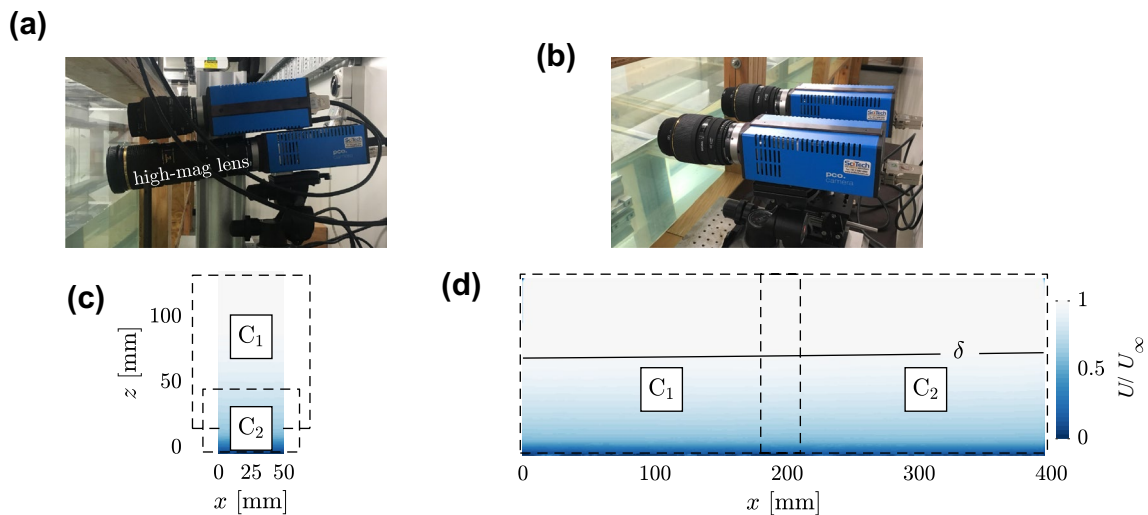
Fig. 4 **a**, **b** Pictures of the cameras showing the arrangements and downward angle of the cameras for the high-magnification and the large FOV measurements, respectively. **c**, **d** The resulting domains from HM-PIV and LF-PIV, respectively, captured by each set-up, overlying the normalised mean velocity field at $U_\infty = 5.6$ m s^{-1}. Dashed boxes in **c**, **d** are the domains captured by the individual cameras. The solid black line in **d** is the boundary layer thickness δ_{99} evolution across the streamwise direction

although within a limited range of λ_x. The wave energy spectra from LF-PIV indicate peak streamwise wavelenghth of about $\lambda_0 \approx 100$ mm, comparable to that extracted from spatiotemporal of Bhirawa et al. (2018) for the same flow case. The steepness of the dominant wave is quantified by $k_0/\lambda_0 = 0.06$.
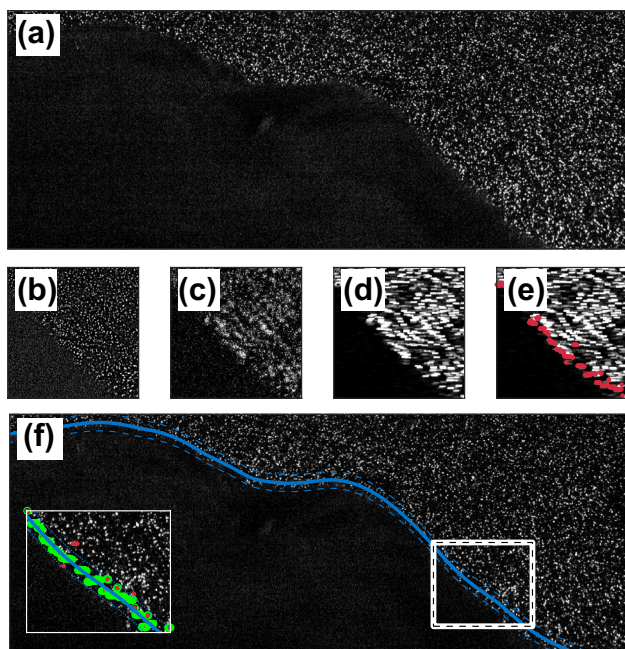
4 Results

4.1 Wave sublayer

Relative to the energy containing motions in the turbulent boundary layer (or atmospheric boundary layer), motions created by waves are significant. Therefore, it is important to investigate the wave-induced motions and their associated role in the turbulent flow. The wall-normal extension of these motions is referred to as "wave boundary layer", WBL. An accurate estimate of the WBL is important, as it affects the outer flow and thus affects the estimate of the friction velocity U_τ (wave drag), as will be discussed in Sect. 4.2. The WBL is usually related to the wave-produced momentum flux away from the waves and extends to multiple dominant wave height k_0, roughly WBL $\approx 3.7k_0$ (Chalikov 1995). To study the induced motions here, we perform a triple decomposition of the velocity (Coceal and Belcher 2004),

$$u_i(x, z, t) = \langle U_i \rangle(z) + \tilde{U}_i(x, z) + u_i'(x, z, t), \quad (1)$$

where u is the instantaneous velocity, i denotes $x-$ or $z-$ directions (e.g. streamwise u or wall-normal w velocity component, respectively), $\langle U \rangle$ is the global mean velocity averaged in x and time t, $\tilde{U}$ is the time-averaged spatial variations about the global mean (wave-induced motions) and u' is the velocity fluctuation. Consequently, our focus is directed towards analysing the flow patterns enveloping a wave crest of the dominant wave, a methodology akin to that executed by Buckley and Veron (2016) and Porchetta et al. (2022). In their analytical work, Buckley and Veron (2016) employed coordinate transformations tailored to the distinct wavelengths of the waves. In contrast, our approach leverages the capabilities of the large FOV measurements of LF-PIV. This facilitates the isolation of the predominant wave through the construction of an averaged representative wave characterised by the wavelength λ_0. To enhance the detecting procedure of the dominant wave, we consider the wave steepness either on the windward $k/\Delta x_W$ or leeward $k/\Delta x_L$ side of the waves, where k represents the wave height and Δx half the wavelength both from the wave crest to trough, as shown in Fig. 7a. This parameter, the wave steepness, is informed by the relationship between wind-generated wave characteristics and wavelength, as summarised by Venugopal and Smith (2007), and validated for the current measurements in Fig. 9. Figure 9 also shows the advantage of the high resolution of the current PIV measurements, where small waves with $\Delta x \lesssim 5$ mm (i.e. $\lambda_x \approx 10$ mm) and $k/\Delta x \lesssim 0.01$ are detected. The selected dominant waves for the current scenario are confined within specific wavelength and wave steepness ranges. Specifically, they fall within the interval of 40 mm $\lesssim \Delta x \lesssim$ 60 mm (approximately equivalent
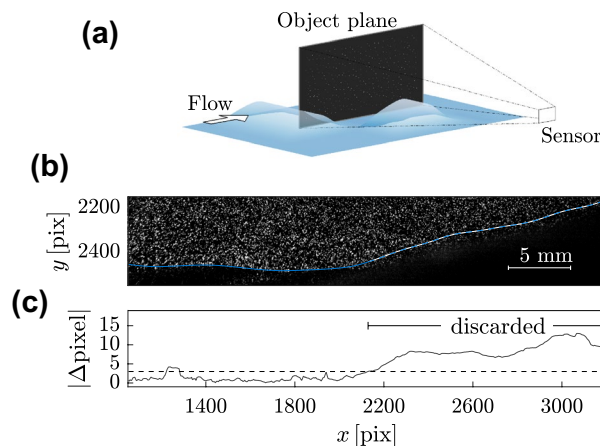
Fig. 5 **a** Raw particle image, **b** image intensity after the high-passed filter, **c** the intensity of the squared values of the previous step, **d** intensity after subsequent Gaussian filter and **e** detected interface for every column, **f** the resulting air–water interface. Solid line: detected surface; dashed lines: ± 0.5 mm. For the inset, red dots are points detected initially; green dots are points used for the final line fit


Fig. 6 **a** Illustration of the view obstruction by a wave crest between the camera sensor and object plane. **b** Sample PIV image showing clear (solid line) and blurry (dashed line) air–water interface. **c** The magnitude of pixel displacement immediately above the detected interface. The black dashed line in **c** is at the threshold of three pixels where velocity data over this line is discarded

to $\pm 10\%$ of the wavelength λ_0) and wave steepness ranging from $0.09 \lesssim k/\Delta x \lesssim 0.16$ (also approximately equivalent to $\pm 10\%$ of the wave number k_0), as delineated by a blue dashed rectangle in Fig. 9. This range has been determined to be sufficient for achieving convergence in $\tilde{U}_i(x,z)$ for the dominant wave analysis.

The variation of all the detected wave instances is illustrated by the series of grey lines in Fig. 10a. The relatively symmetric wave shape, shown with a black solid line in Fig. 10a, is a result of averaging the different steepness waves (grey lines). A total of approximately 120 instances are used to construct the mean wave shape and to compute the velocity statistics. Figure 10b, c depicts the time-averaged spatial variations $\tilde{U}_0$ and $\tilde{W}_0$. The subscript '0' signifies that the averaging is conditioned only on the dominant waves. The horizontal and vertical axes of these figures are referenced to the location of the wave peak, where $\Delta x = 0$ and $\Delta z = 0$ correspond to the peak position (marked with a '+').

Figure 10b shows characteristic separation, manifested by a pronounced negative value of $\tilde{U}_0 < 0$ on the leeward side of the averaged wave profile. Comparable to observations in flow over rough surfaces, Fig. 10b reveals that the variations of $\tilde{U}_0$ across the analysed waves predominantly cluster near the wave crest and immediately below it. These localised separation regions extend to an approximate distance

of $\Delta z \approx 6$ mm downwind of the wave's crest, beyond which they attenuate (i.e. becoming negligibly small with $\tilde{U}_0 \lesssim 0.01$), and the flow becomes relatively uniform. Conversely, the spatial disparities of $\tilde{W}_0$ appear to extend to a higher wall-normal location, approximately $\Delta z \approx 60$ mm above the wave crest, as depicted in Fig. 10c. This notable wall-normal elongation of $\tilde{W}_0$ could be attributed to the circumstance where λ_x approaches a comparable scale to the boundary layer thickness δ. Nugroho et al. (2021) illustrated that in such cases, the motions due to roughness could extend through the lower half of the boundary layer, potentially influencing the dynamics in the logarithmic region and resulting in a lack of outer-layer similarity. The thickness of the WBL for the dominant waves (WBL$_0$) is determined based on the attenuation of the dispersive component of Reynolds stress, denoted as $\langle \tilde{U}_0 \tilde{W}_0 \rangle$ (Buckley and Veron 2016). This attenuation is observed at WBL$_0 \approx 17$ mm, which is approximately equivalent to $2k_0$. However, it is important to note that this limit, which represents the wall-normal extension of the wave effect in the flow, is computed only for the dominant waves. In reality, the wall-normal extension of the wind wave effect is likely smaller due to the presence of various wave scales, as illustrated in Fig. 8 and discussed in the following section.
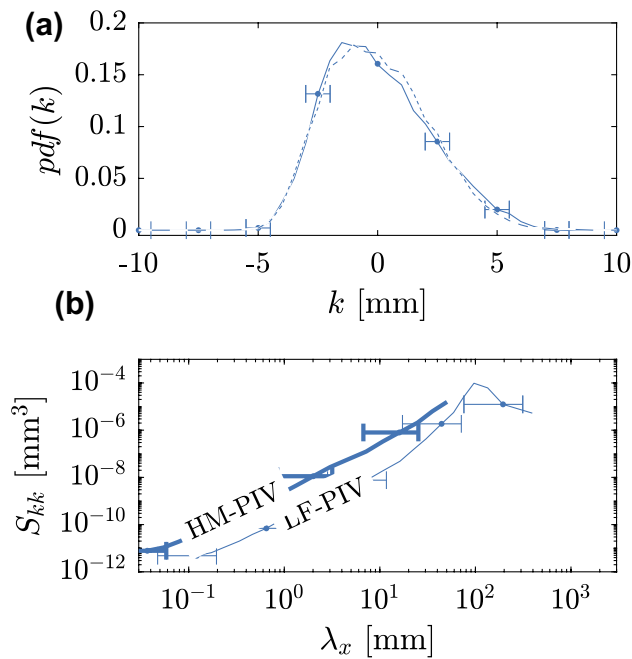
4.2 Estimation of friction velocity

In assessing the friction velocity U_τ, two commonly used methodologies are the Clauser method and the total shear stress method. While these approaches have been validated in the context of flows over rough surfaces, their application to flows over waves introduces certain complexities.

(a)

(b)
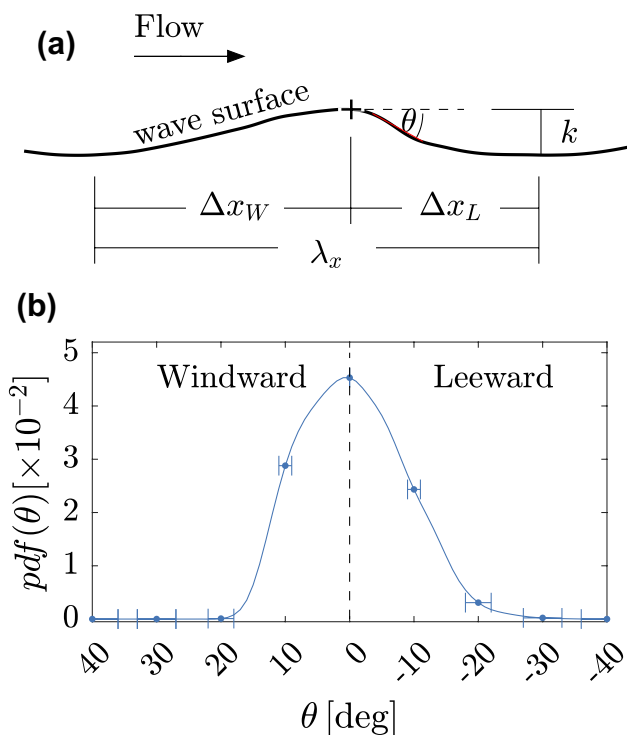
Fig. 7 **a** Illustration of wave asymmetry analysis using the wave angle θ measured from the horizontal line and tangent along the wave surface. Here, k and λ_x denote the wave height and wavelength, respectively. The streamwise distances from the wave crest to trough in both windward and leeward sides, Δx_W and Δx_L, are also annotated in **a** and will be used in the analysis of wave steepness in Sect. 4.1. **b** The probability density function (*pdf*) of θ is shown in **b**. The vertical dashed line at $\theta = 0°$ represents the reference line, with positive and negative values of θ corresponding to the windward and leeward sides of the waves. The error bars in **b** represent the uncertainty in wave detection of HM-PIV system

(a)

(b)

Fig. 8 **a** Probability density function of the wave-height fluctuation, *pdf*(*k*). Solid and dashed lines: data from HM-PIV and the reference ultrasonic sensor, respectively. **b** Power spectral density S_{kk} as a function of streamwise wavelength λ_x. Thick and thin lines in **b** indicate the HM-PIV and LF-PIV data, respectively. The error bars in **a**, **b** indicate the uncertainty associated with each respective measurement technique

Notably, in laboratory-scale facilities, where the wave height is significant relative to the boundary layer thickness (k_0/δ, referred to as the blockage ratio), the wave effects can extend into the outer flow region. This aspect is often overlooked in the existing literature on air–wave interactions, potentially affecting the applicability of the outer-layer similarity assumption. This assumption posits that turbulence behaves similarly away from the wall over both smooth and rough surfaces, encompassing the universal logarithmic region and the "wake" of the boundary layer (Townsend 1976; Raupach et al. 1991; Jiménez 2004). Typically, for similarity to hold, a sufficiently small value of $k/\delta \lesssim 0.03$ is required (Jiménez 2004). In the case of the Clauser method, another challenge arises from the significant variations in wave height, which introduce uncertainties in determining the virtual origin, a theoretical point within the boundary layer characterised by approaching zero velocity and pressure. Therefore, in this section, we explore the influence of waves on estimating U_τ

and highlight potential uncertainties associated with both the Clauser method and the total shear stress method.

The estimation of U_τ in turbulent boundary layers along smooth walls is typically carried out by fitting mean velocity data within the logarithmic region to the log-law $U_{\log}^+ = \kappa^{-1} \log(z^+) + A$, where '+' denotes normalisation with U_τ and v, and $\kappa = 0.38$ and $A \approx 4.2$ are the log-law constants. However, in cases involving rough walls and waves (Chung et al. 2021; Geva and Shemer 2022), the mean velocity profile within the logarithmic region shifts downward compared to the profile for smooth walls by the roughness function, $\Delta U^+ = \Delta U/U_\tau$ (Hama 1954). Consequently, a modified logarithmic profile ($U_{\log}^+ - \Delta U^+$) is employed. In this scenario, the friction velocity is determined as the value that yields a slope (κ) in the logarithmic region comparable to that of a smooth wall.

In Fig. 11a, the viscous-scaled mean streamwise velocity ($\langle U \rangle^+ = \langle U \rangle / U_\tau$) is plotted against the viscous-scaled wall-normal height ($z^+ = z/U_\tau$). In this plot, we assume the virtual origin ($z = 0$) corresponds to the stationary water surface level. The plot includes mean profiles from zero-pressure gradient boundary layer direct numerical simulations by Sillero et al. (2013) at $Re_\tau \approx 1300$ and 2000,

as well as $U_{\log}^+$, where $Re_\tau = \delta U_\tau/\nu$ represents the friction Reynolds number, and δ is the boundary layer thickness.

Typically, in smooth wall boundary layers, the wall-normal extension of the logarithmic region is limited to $3.6\sqrt{Re_\tau} \lesssim z^+ \lesssim 0.20 Re_\tau$ (Marusic et al. 2013; Morrill-Winter et al. 2017). However, in the presence of a non-smooth wall, such as waves in this case, the wall effect could extend to a higher wall-normal location compared to a smooth wall. Here, we initially utilise the wave boundary layer for the dominant waves, WBL_0, as the lower limit of the logarithmic region. The viscous-scaled $WBL_0^+ \approx 440$ from the stationary water surface level exceeds the upper limit of the logarithmic region $0.20 Re_\tau \approx 345$ from the stationary water surface level, indicating no logarithmic region, i.e. 'healthy' turbulence (Flores and Jiménez 2010), penetrating deeper into the outer layer. This observation is also supported by a relatively large blockage ratio, approximately $k_0/\delta \approx 0.10$, compared to the required $k/\delta \lesssim 0.03$ for outer-layer similarity to hold. However, an interesting observation in Fig. 11a is the persistence of a log-linear trend below WBL_0. This finding confirms that the induced motion by the wind waves, which can influence turbulence below the traditional logarithmic region, extends to a wall-normal distance smaller than WBL_0. In the current scenario, it becomes apparent that the lower boundary of the logarithmic region initiates at approximately $z^+ \approx 200$. This insight is supported by the flat region observed in the indicator function ($\beta = z^+ dU^+/dz^+$) in the inset of Fig. 11a. Collectively, these results imply that the wind-generated WBL in cases with a wide range of wave structures (see Fig. 8b) cannot be solely attributed to the dominant wave but may involve a WBL influenced by motions generated by waves of various scales. We determine U_τ as the value that provides the best fit to the slope of the log-law. We find U_τ to be 0.312 m s^{-1}, corresponding to $Re_\tau \approx 1750$ where $\delta \approx 84$ mm.

To further validate our current estimate of U_τ, we utilise the total shear stress method, which assumes a region of constant shear stress equal to the wall shear stress in the overlap and inner region of the boundary layer (Krogstad et al. 1992; Janssen 2004; Flack et al. 2005). This method allows us to determine the friction velocity as

$$U_\tau \simeq \sqrt{\nu \frac{\partial\langle U\rangle}{\partial z} - \langle u'w'\rangle}, \qquad (2)$$

where the first term on the right-hand side, $\nu(\partial U/\partial z)$, represents the viscous stress, which is negligible far from the wall compared to the second term $\langle u'w'\rangle$, representing the Reynolds shear stress, for a fully rough surface. Figure 11b presents the normalised Reynolds shear stress profiles, $\langle u'w'\rangle^+$, where the data from turbulent boundary layers over a flat plate from Sillero et al. (2013) are included for comparison.
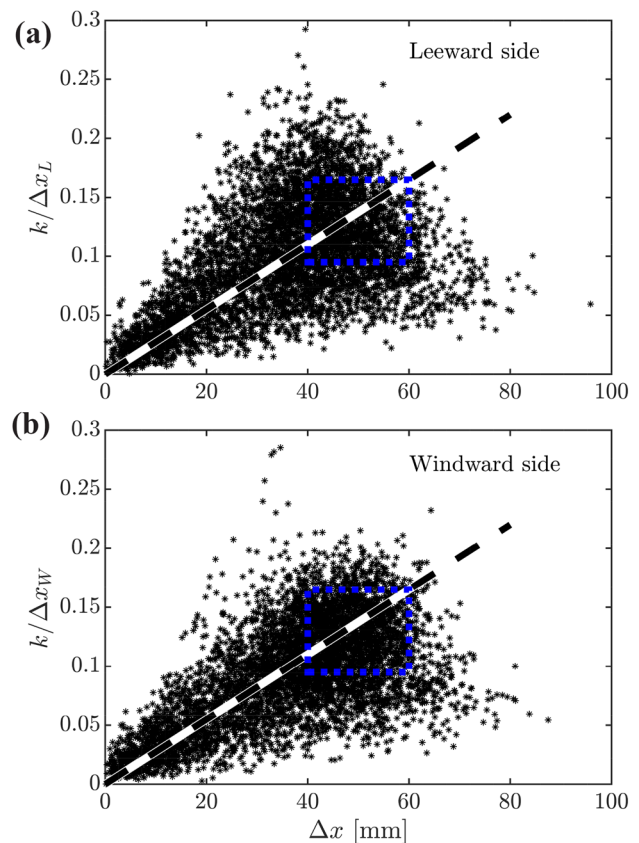
Fig. 9 The relation between the ascertained wavelength of detected waves, denoted as Δx, and their corresponding steepness **a** on the leeward ($k/\Delta x_L$) and **b** windward ($k/\Delta x_W$) sides of the identified waves. The dashed black line delineates a linear regression illustrating the relation between wave steepness and wavelength. The dotted blue rectangle delineates a specific region from which the waves were selected for presentation in Fig. 10

In the data obtained from the flat plate, a relatively constant region with $-\langle u'w'\rangle^+ \approx 1$ is observed, as shown in Fig. 11b. As the Reynolds number increases, this plateau is expected to extend, signifying the thickening of the logarithmic region. However, in flows over large roughness elements, especially at lower Reynolds numbers, this constant shear stress region might not be immediately evident from the "inner bump" caused by separation events. To utilise Eq. (2), we consider the $\langle u'w'\rangle$ values at elevations above the roughness height. It is worth noting that a similar small plateau with $-\langle u'w'\rangle^+ \approx 1$ can also be observed in DNS studies of flows over large roughness elements, as demonstrated by Coceal et al. (2007) and Lee et al. (2011), where turbulence is fully resolved. The calculated U_τ value from this technique is 0.281 m s^{-1}, which is 12% less than that estimated using the Clauser method. It is worth noting here that in the two discussed techniques, the wall-normal virtual origin is considered at the stationary water surface level, and thus,
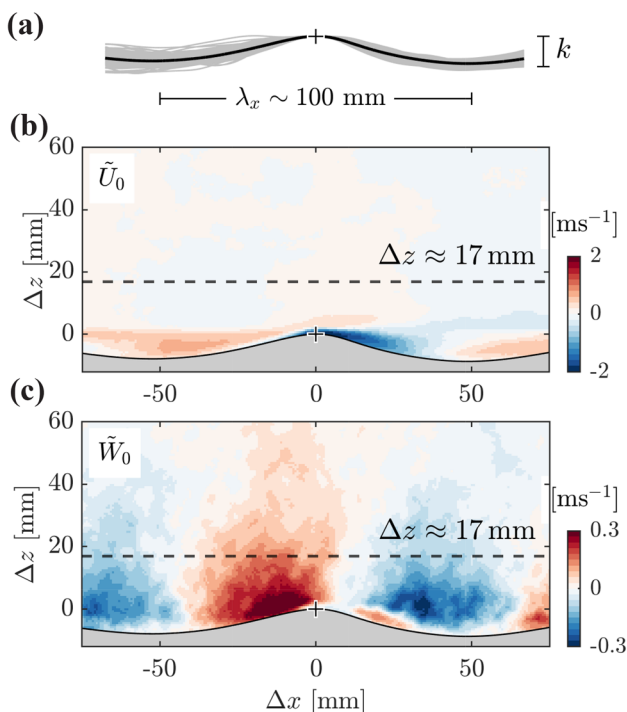
Fig. 10 a Illustration of the dominate wave detection (grey lines) and average wave geometry (black line), **b**, **c** contour of the streamwise $\tilde{U}_0$ and wall-normal $\tilde{W}_0$ time-averaged spatial variations of the dominating wave for $U_\infty = 5.6$ m s^{-1}. The dashed lines in **b**, **c** present the WBL$_0$ estimated where $\langle \tilde{U}_0 \tilde{W}_0 \rangle$ becomes smaller than 0.01 when averaged in x

larger error might be encountered due to the uncertainty of determining the virtual origin for air generated waves with wide spectrum of wave scales and due to large blockage ration. Thus, close considerations of the virtual origin, the blockage ratio k_0/δ and detailed measurement in the vicinity of the waves are required for flow measurements over waves in laboratory settings to limit the uncertainty of estimating U_τ and the associated parameters.

4.3 The effect of spatial resolution on vorticity near the capillary-gravity waves

The interaction between wind and waves entails a continuous exchange of energy across various wave scales (Longuet-Higgins 1969; Hasselmann 1971), resulting in the generation of new wind waves. This dynamic process manifests notably through the emergence of ripples, characterised by the development of high-vorticity areas on the leeward side of individual waves, as demonstrated in recent simulations by Matsuda et al. (2023). To discuss this phenomenon, we plot in Fig. 12a the spanwise vorticity ω_y in the vicinity of a steep primary wave. The presence of a distinct shear layer is clear
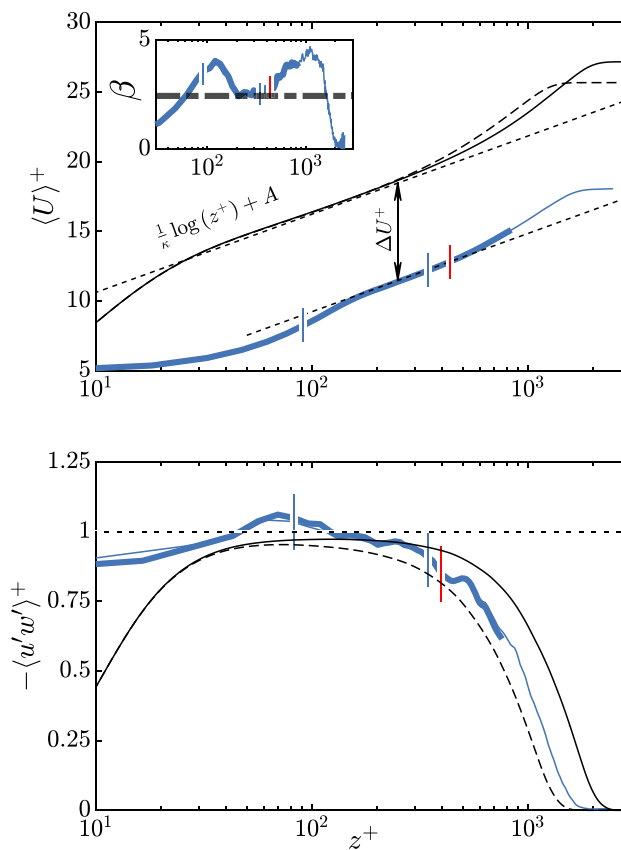
Fig. 11 a Viscous-normalised mean streamwise velocity $\langle U \rangle^+$ and **b** viscous-normalised Reynolds shear stress $\langle u'w' \rangle^+$ versus the viscous-scaled wall-normal distance z^+. Here, $z = 0$ corresponds to the stationary water surface level. The vertical lines in **a** and **b** from left to right are at the dominant wave peak k_0^+ (at $z^+ \approx 91$ from the stationary water surface level), the upper limit of the logarithmic region ($0.20Re_\tau$) and the WBL$_0$ (shown in red). The black solid and dashed lines are data of the zero-pressure-gradient flat plate by Sillero et al. (2013) at $Re_\tau \approx 1300$ and 2000. In **a**, the black dotted line is the log-law U_{log}^+, while the coloured dotted lines are the modified log-law $U_{\mathrm{log}}^+ - \Delta U^+$. The inset in **a** shows the indicator function ($\beta = z^+ \mathrm{d}U^+/\mathrm{d}z^+$) while the dot-dashed line is at κ^{-1}. The black dotted line in **b** is at $-\langle u'w' \rangle^+ = 1$

from the deviation of the ω_y contour from the wave surface, forming an almost horizontal shear layer at the edge of the dominant wave. This observation is consistent with previous studies by Veron et al. (2007), Reul et al. (2008) and Buckley and Veron (2016). This shear layer is accompanied by a noticeable vorticity field. This field is further illustrated with the swirling strength values Ω_y in Fig. 12b. The swirl strength here is defined as the imaginary part of the complex eigenvalue of the two-dimensional velocity gradient tensor following Adrian et al. (2000), providing insight into the vortex core that penetrates the measurement plane. Figure 12b clearly shows the eddies shed during the initial separation

event along the high-shear region. Although these separation events from the dominate wave are typically an indication of the onset of wave breaking (or folding) (Banner and Melville 1976) for deformable water surface, for shorter waves of approximately 0.1 m, this folding can still be prevented by surface tension (Kawai 1981; Banner and Peregrine 1993).

The influence of the emerged ripples on the flow at the leeward side of the dominant wave is highlighted within dashed rectangles in Fig. 12a, b. In this region, significant separation-induced vortical activities occur due to the presence of capillary waves (ripples). The connection between these separation-induced vortical activities and the presence of ripples is also evident from the simulations of Matsuda et al. (2023), where they demonstrated that suppressing the ripples by altering surface tension also led to a suppression of significant vortical activities. These separation-induced vortices are likely to influence overall surface drag and further enhance gas and/or heat transfer across the air–sea interface (Melville 1996).

The discussion regarding Fig. 12a, b emphasises the influence of ripple trains generated on steeper waves, which is captured from the high resolution of the current PIV system. For example, vortical activities of sizes on the order of 10 wall units (comparable to the smallest capillary waves with wavelengths of 0.3 mm Zhang 1995) are captured as shown in the inset of Fig. 12b. To demonstrate the impact of spatial resolution on the attenuation of these high-vorticity events, we present the spanwise vorticity ω_y in Fig. 12c, e and the swirling strength in Fig. 12d, f, following spatial averaging of the velocity field using box filters of dimensions $\Delta x_i^+ \approx 10 \times 10$ in (c, d) and 30×30 in (e, f). It is important to note that the box filter of $\Delta x_i^+ \approx 10 \times 10$ is proximate to the size of the smallest capillary waves of 0.3 mm as suggested by Zhang (1995). A similar approach of altering spatial averaging was previously employed in numerical simulations conducted by Hung and Tsai (2009). In their study, computational grid points were incrementally increased until computed surface elevation and velocity fields exhibited alterations in response to changes in grid resolution.

As illustrated in Fig. 12c, e, ω_y and Ω_y originating from the carrier wave edge appear unaffected by spatial resolution of $\Delta x_i^+ \approx 10 \times 10$, presumably due to vortex size larger than the box filter. However, smaller vortices, such as those generated by ripples (within the dashed rectangle in Fig. 12c) and the inset of Fig. 12d, are attenuated. The attenuation in spanwise vorticity at the leeward side of multiple dominant waves (e.g. Fig. 12c) compared to the unfiltered case (e.g. Fig. 12a) is estimated at nearly 35%. Further increase in spatial averaging, e.g. 30×30 in Fig. 12e, f, leads to approximately 80% attenuation of vortices at the leeward side of the dominant wave compared to the unfiltered case, as also could be inferred from loss of small vorticity in the inset of Fig. 12f.

From these findings, we can infer that due to the multi-scale nature of wind-generated waves, spatial resolution of approximately the order of capillary waves is required in the vicinity of waves to adequately account for the contribution of capillary waves to wind flow.

5 Conclusion

Geophysical forces, such as oceanic winds, generate a diverse range of wave scales, spanning from capillary-gravity waves to longer sea swells. To comprehend the impact of these waves on airflow characteristics, particularly small-scale waves, controlled laboratory experiments are essential. Particle image velocimetry (PIV) serves as a valuable tool in this regard, yet its application over moving waves, particularly multi-scale wind-generated waves, presents challenges, including the influence of measurement resolution on results and wave surface detection from PIV images.

To address these challenges, we conducted two PIV experiments under identical wind-wave conditions. The first utilised high-magnification set-up to capture turbulent motions near the wave surface within a confined streamwise–wall-normal plane, enabling an examination of spatial resolution effects. The second experiment employed a large field-of-view (FOV) to study flow over consecutive waveforms and obtain spatial averages.

Our findings broadly align with the existing literature, revealing the formation of a horizontal shear layer leading to airflow separation on the lee side of the wave, accompanied by pronounced vorticity fields and circulation regions. Analysis of high-magnification datasets, however, unveiled localised airflow separation induced by small-scale capillary waves, a phenomenon not resolved by the large FOV set-up. This finding underscores the critical importance of adequate spatial resolution in capturing subtle airflow dynamics near the wave surface. Systematic spatial averaging of the velocity field of the high-magnification dataset suggests that a resolution of approximately the size of the capillary waves is required to capture the contribution of capillary waves to the wind flow.

From previous studies, wave surface detection for PIV measurements required additional imaging systems, such as laser-induced fluorescence or cameras detecting the dyed water surface. In our study, we introduce a novel method relying solely on PIV images to identify wave surfaces, demonstrating its effectiveness in detecting capillary-scale waves.

Appendix A: Uncertainty analysis

Given the complex nature of the measurement process, involving number of equipment and processing stages, it is expected that uncertainty arises from multiple sources. These sources are classified into two main categories: measurement uncertainty, which pertains to potential deviations arising from equipment precision, and processing uncertainty, which stems from data manipulation procedures such as wave surface detection or friction velocity determination. Typically, for parameters with explicit expressions and straightforward partial derivatives (e.g. freestream velocity $U_\infty = \sqrt{2\Delta p/\rho}$, where Δp represents the differential pressure measured by the Pitot tube and ρ denotes air density), uncertainty analysis is conducted by estimating the

percentage of uncertainty through the propagation of error method as

$$\epsilon(X) = \left[\sum_{i=1}^{N} \left(\frac{\partial X}{\partial A_i} \epsilon(A_i) \right)^2 \right]^{1/2}, \tag{3}$$

where ϵ is the error of a parameter, X is the parameter that we wish to obtain the error for, $\frac{\partial X}{\partial A_i}$ is the partial derivative of X with respect to A_i where A_i is a variable that X depends on (i.e. $X = f(A_i)$) and N is the number of variables. However, when dealing with quantities realised through multiple processing steps or calculations (e.g. estimating the friction velocity), a more generalised technique of error estimation is recommended, as proposed by Moffat (1988) through

$$\epsilon(X) = \left[\sum_{i=1}^{N} \left[X(A_i \pm \epsilon(A_i)) - X(A_i) \right]^2 \right]^{1/2}, \tag{4}$$

where A_i is a variable on which X depends, and $\epsilon(A_i)$ is the uncertainty in that variable. It is important to note that based on the expressions in (3) and (4), if the uncertainty of each parameter $\epsilon(X)$ is expanded, the resulting uncertainty $\epsilon(X)$ will also be expanded. Explanations regarding the application of (3) and (4), along with the anticipated uncertainty, can be found in Abu Rowin et al. (in press). Table 2 shows the uncertainty associated with each parameter presented in the main body of this work. As detailed in this table, the
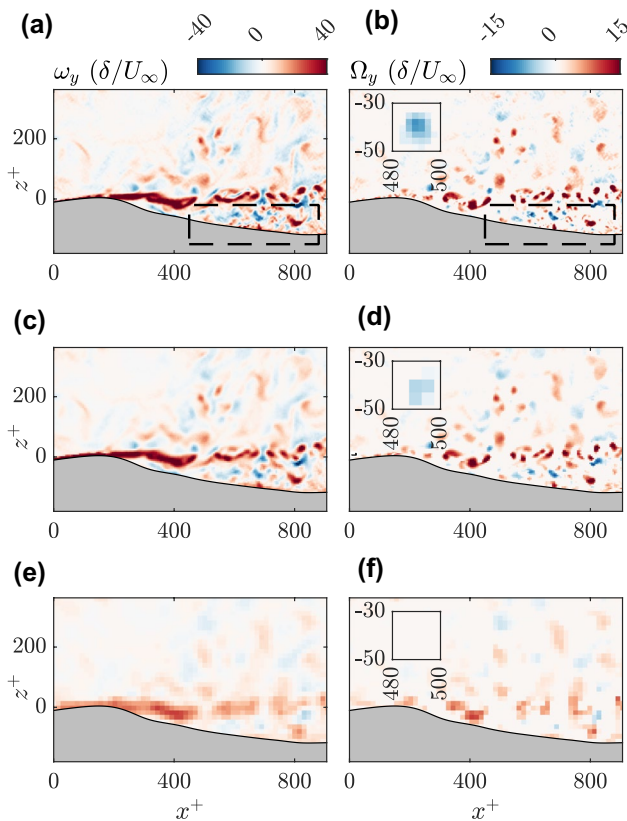
Fig. 12 Spanwise vorticity ω_y (**a**, **c**, **e**) and swirling strength Ω_y (**b**, **d**, **f**) fields normalised by the boundary layer thickness δ and freestream velocity U_∞ for an instantaneous flow field event. The plots from top to bottom are processed with larger box filter of ($\Delta x_i^+ \approx$) (**a**, **b**) 5×5, (**c**, **d**) 10×10 and (**e**, **f**) 30×30 in the streamwise and wall-normal directions, to resemble the effect of the spatial resolution. The dashed rectangles in **a**, **b** highlight the spanwise vorticity generated by the small-scale waves. The insets in **b**, **d**, **f** show a zoomed-in view of a vortex imposed by the small-scale waves attenuated with different box filter sizes

Table 2 Uncertainties for parameters presented in this study were obtained either directly from the manufacturers or computed using (3) and (4)

Parameter	Unit	ϵ	Method
k	mm	0.18	Manufacturer[a]
k	mm	0.58	(4)[b]
k	mm	0.61	(4)[c]
p	%	0.25	Manufacturer
ρ	kg m^{-3}	0.0007	(3)
U_∞	mm s^{-1}	125	(3)
C_p	–	0.04	(3)
U_τ	m s^{-1}	0.02	(4)[d]
U_τ	m s^{-1}	0.01	(4)[e]
ΔU^+	–	1.03	(4)[d]
ΔU^+	–	0.52	(4)[e]

[a] The uncertainty of the wave height (k) from the ultrasonic sensor

[b] The uncertainty of k including the resolution of HM-PIV system and surface detection

[c] The uncertainty of k including the resolution of LF-PIV system and surface detection

[d] Uncertainty owing to the use of Clauser fit

[e] Uncertainty owing to the use of the total shear stress method

uncertainties are directly obtained from the manufacturer or computed using (3) or (4). The figures presented in the main body of this work feature error bars reflecting the uncertainty listed in Table 2.

Declarations

References

Abu Rowin W, Kevin (2023) Determining air–water interface code. https://github.com/Aburowin/air_water_interface

Abu Rowin W, Xia Y, Wang S, Hutchins N (2024) Accurately predicting turbulent heat transfer over rough walls: a review of measurement equipment and methods. Exp Fluids. https://doi.org/10.1007/s00348-024-03812-1

Adrian RJ, Christensen KT, Liu ZC (2000) Analysis and interpretation of instantaneous turbulent velocity fields. Exp Fluids 29(3):275–290

Astarita T, Cardone G (2005) Analysis of interpolation schemes for image deformation methods in PIV. Exp Fluids 38:233–243

Atkinson C, Buchmann NA, Amili O, Soria J (2014) On the appropriate filtering of PIV measurements of turbulent shear flows. Exp Fluids 55(1):1654

Banner M, Peirson WL (1998) Tangential stress beneath wind-driven air–water interfaces. J Fluid Mech 364:115–145

Banner ML, Melville WK (1976) On the separation of air flow over water waves. J Fluid Mech 77:825–842

Banner ML, Peregrine DH (1993) Wave breaking in deep water. Annu Rev Fluid Mech 25(1):373–397

Barger WR, Garrett WD, Ruggles ELM-CKW (1970) Effects of an artificial sea slick upon the atmosphere and the ocean. J Appl Meteorol 9(3):396–400

Bhirawa T, Kevin, Lee JH, Monty JP (2018) Time-resolved spatial measurements of gravity-capillary waves. In: 21st Australasian fluid mechanics conference, Perth, Australia

Buckley MP, Veron F (2016) Structure of the airflow above surface waves. J Phys Ocean 46(5):1377–1397

Buckley MP, Veron F (2017) Airflow measurements at a wavy air–water interface using PIV and LIF. Exp Fluids 58(11):161

Chalikov D (1995) The parameterization of the wave boundary layer. J Phys Ocean 25(6):1333–1349

Chung D, Hutchins N, Schultz MP, Flack KA (2021) Predicting the drag of rough surfaces. Annu Rev Fluid Mech 53:439–471

Coceal O, Belcher SE (2004) A canopy model of mean winds through urban areas. Q J R Meteorol Soc 130(599):1349–1372

Coceal O, Dobre A, Thomas TG, Belcher SE (2007) Structure of turbulent flow over regular arrays of cubical roughness. J Fluid Mech 589:375–409

Donelan MA, Haus BK, Reul N, Plant WJ, Stiassnie M, Graber HC, Brown OB, Saltzman ES (2004) On the limiting aerodynamic roughness of the ocean in very strong winds. Geophys Res Lett 31(18):1–5

Dussol D, Druault P, Mallat B, Delacroix S, Germain G (2016) Automatic dynamic mask extraction for PIV images containing an unsteady interface, bubbles, and a moving structure. C R Mécanique 344(7):464–478

Flack KA, Schultz MP, Shapiro TA (2005) Experimental support for Townsend's Reynolds number similarity hypothesis on rough walls. Phys Fluids 17(3):035102

Flores O, Jiménez J (2010) Hierarchy of minimal flow units in the logarithmic layer. Phys Fluids 22(7):071704

Geva M, Shemer L (2022) Wall similarity in turbulent boundary layers over wind waves. J Fluid Mech 935:A42

Grare L, Peirson WL, Branger H, Walker JW, Giovanangeli J-P, Makin V (2013) Growth and dissipation of wind-forced, deep-water waves. J Fluid Mech 722:5–50

Hama FR (1954) Boundary layer characteristics for smooth and rough surfaces. Trans Soc Nav Arch Mar Eng 62:333–358

Harun Z, Monty JP, Mathis R, Marusic I (2013) Pressure gradient effects on the large-scale structure of turbulent boundary layers. J Fluid Mech 715:477–498

Hasselmann K (1971) On the mass and momentum transfer between short gravity waves and larger-scale motions. J Fluid Mech 50:189–205

Holthuijsen LH (2010) Waves in oceanic and coastal waters. Cambridge University Press, Cambridge

Hung L-P, Tsai W-T (2009) The formation of parasitic capillary ripples on gravity-capillary waves and the underlying vortical structures. J Phys Ocean 39(2):263–289

Janssen P (2004) The interaction of ocean waves and wind. Cambridge University Press, Cambridge

Jeon YJ, Sung HJ (2011) PIV measurement of flow around an arbitrarily moving body. Exp Fluids 50:787–798

Jiménez J (2004) Turbulent flows over rough walls. Annu Rev Fluid Mech 36:173–196

Kähler CJ, Scharnowski S, Cierpka C (2012) On the uncertainty of digital PIV and PTV near walls. Exp Fluids 52:1641–1656

Kawai S (1981) Visualization of airflow separation over wind-wave crests under moderate wind. Bound-Layer Meteorol 21(1):93–104

Kevin, Monty JP, Hutchins N (2019) Turbulent structures in a statistically three-dimensional boundary layer. J Fluid Mech 859:543–565

Krogstad P-Å, Antonia RA, Browne LWB (1992) Comparison between rough-and smooth-wall turbulent boundary layers. J Fluid Mech 245:599–617

Laxague NJ, Haus BK, Bogucki D, Özgökmen T (2015) Spectral characterization of fine-scale wind waves using shipboard optical polarimetry. J Geophys Res Oceans 120:3140–3156

Lecordier B, Demare D, Vervisch L, Réveillon J, Trinite M (2001) Estimation of the accuracy of PIV treatments for turbulent flow studies by direct numerical simulation of multi-phase flow. Meas Sci Technol 12(9):1382

Lee JH, Sung HJ, Krogstad P-Å (2011) Direct numerical simulation of the turbulent boundary layer over a cube-roughened wall. J Fluid Mech 669:397–431

Lin H, Perlin M (1998) Improved methods for thin, surface boundary layer investigations. Exp Fluids 25(5):431–444

Lin H, Perlin M (2001) The velocity and vorticity fields beneath gravity-capillary waves exhibiting parasitic ripples. Wave Motion 33(3):245–257

Liu P, Al-Banaa K, Cowen E (2004) Water wave induced boundary layer flows above a ripple bed. In: Grue J (ed) PIV and water waves. World Scientific, Singapore, pp 81–117

Longuet-Higgins MS (1969) A nonlinear mechanism for the generation of sea waves. Proc R Soc A 311:371–389

Longuet-Higgins MS (1987) The propagation of short surface waves on longer gravity. J Fluid Mech 177:293–306

Longuet-Higgins MS (1992) Capillary rollers and bores. J Fluid Mech 240:659–679

Marusic I, Monty JP, Hultmark M, Smits AJ (2013) On the logarithmic region in wall turbulence. J Fluid Mech 716:R3

Matsuda K, Komori S, Takagaki N, Onishi R (2023) Effects of surface tension reduction on wind-wave growth and air–water scalar transfer. J Fluid Mech 960:A22

Melville WK (1996) The role of surface-wave breaking in air-sea interaction. Annu Rev Fluid Mech 28:279–321

Moffat R (1988) Describing the uncertainties in experimental results. Exp Therm Fluids Sci 1(1):3–17

Morrill-Winter C, Philip J, Klewicki J (2017) An invariant representation of mean inertia: theoretical basis for a log law in turbulent boundary layers. J Fluid Mech 813:594–617

Mueller JA, Veron F (2009) Nonlinear formulation of the bulk surface stress over breaking waves: feedback mechanisms from air-flow separation. Exp Fluids 130:117–134

Mui R, Dommermuth DG (1995) The vortical structure of parasitic capillary waves. J Fluids Eng 117:355–361

Nugroho B, Monty J, Utama I, Ganapathisubramani B, Hutchins N (2021) Non-type behaviour of roughness when in-plane wavelength approaches the boundary layer thickness. J Fluid Mech 911:A1

Okuda K (1982) Internal flow structure of short wind waves: Part I. On the internal vorticity structure. J Oceanogr Soc Japan 38:28–42

Pizzo N, Deike L, Ayet A (2021) How does the wind generate waves? Phys Today 74(11):38–43

Porchetta S, Carlesi T, Rosaria MV, van Beeck J, Laboureur D (2022) Experimental investigation of the airflow structure above mechanically generated regular waves for both aligned and opposed wind-wave directions. Exp Therm Fluid Sci 133:110578

Raupach MR, Antonia RA, Rajagopalan S (1991) Rough-wall turbulent boundary layers. Appl Mech Rev 44(1):1–25

Reul N, Branger H, Giovanangeli JP (1999) Air flow separation over unsteady breaking waves. Phys Fluids 11(7):1959–1961

Reul N, Branger H, Giovanangeli J-P (2008) Air flow structure over short-gravity breaking water waves. Bound-Layer Meteorol 126(3):477–505

Sanchis A, Jensen A (2011) Dynamic masking of PIV images using the radon transform in free surface flows. Exp Fluids 51:871–880

Sciacchitano A, Wieneke B (2016) PIV uncertainty propagation. Meas Sci Technol 27(8):084006

Sillero JA, Jiménez J, Moser RD (2013) One-point statistics for turbulent wall-bounded flows at Reynolds numbers up to $\delta^+ \approx 2000$. Phys Fluids 25(10):105102

Stanislaw M (2012) Ocean surface waves: their physics and prediction, 2nd edn. World Scientific, Singapore

Sullivan PP, McWilliams JC (2010) Dynamics of winds and currents coupled to surface waves. Annu Rev Fluid Mech 42:19–42

Sveen JK, Jensen A (2004) PIV methods, boundary layer flows and turbulence. PIV Water Waves 9:301

Townsend AA (1976) The structure of turbulent shear flow, 2nd edn. Cambridge University Press, Cambridge

Venugopal V, Smith GH (2007) The effect of wave period filtering on wave power extraction and device tuning. Ocean Eng 34(8–9):1120–1137

Veron F, Saxena G, Misra SK (2007) Measurements of the viscous tangential stress in the airflow above wind waves. Geophys Res Lett. https://doi.org/10.1029/2007GL031242

Zarruk G (1970) Measurement of free surface deformation in PIV images. Meas Sci Technol 16(10):2005

Zhang X (1995) Capillary-gravity and capillary waves generated in a wind wave tank: observations and theories. J Fluid Mech 289:51–82